Journal of Materials Chemistry A

ROYAL SOCIETY OF CHEMISTRY

PAPER

View Article Online
View Journal | View Issue

Cite this: *J. Mater. Chem. A*, 2022, **10**, 19710

Atomically miniaturized bi-phase IrO_x/Ir catalysts loaded on N-doped carbon nanotubes for high-performance Li–CO_2 batteries†

Yeo-Jin Rho,‡[a] Boran Kim,‡[a] Kihyun Shin,‡[b] Graeme Henkelman[b] and Won-Hee Ryu*[a]

Li–CO_2 batteries are bifunctional, spontaneously storing energy and fixing environmental CO_2 without external electricity. Identifying efficient catalysts that can accelerate the reversible formation and decomposition of the insulating carbonate products formed on the electrode remains challenging. To overcome this limitation, we atomically dispersed IrO_x/Ir bi-phase particles as single-atom catalysts (SACs) on nitrogen-doped carbon nanotubes (NCNTs) and introduced them to facilitate a reversible Li–CO_2 reaction with low overpotential and stable cycle performance for 120 cycles. The IrO_x/Ir SACs were successfully minimized to an atomic scale of 4 Å and formed unique surface oxides *via* dangling bonds on the atomic Ir catalyst, enhancing the surface catalytic activities. The N sites doped on the carbon nanotubes increased the electronic conductivity and provided favorable nucleation sites for Ir loading. The Li–CO_2 cells employing IrO_x/Ir SACs loaded on NCNTs exhibited improved cell performance, reduced polarization, lower charge transfer resistance, and higher stable cyclability compared to cells employing larger-sized Ir particles on NCNTs. The reversible Li–CO_2 reaction mechanism facilitated by the IrO_x/Ir SAC-loaded NCNT catalyst is explained through density functional theory (DFT) calculations that demonstrated that the bond of SACs with ($Li^+ + e^-$) is strong and forms products, whereas the bond with $Li_2CO_3^*$ is weak and evolves products reversibly. This strategy to atomically minimize noble metal catalysts may facilitate the realization of high-performance and economical Li–CO_2 batteries to achieve carbon-negativity targets.

Received 21st March 2022
Accepted 23rd May 2022

DOI: 10.1039/d2ta02234f

rsc.li/materials-a

[a]*Department of Chemical and Biological Engineering, Sookmyung Women's University, 100 Cheongpa-ro 47-gil, Yongsan-gu, Seoul, 04310, Republic of Korea. E-mail: whryu@sookmyung.ac.kr*

[b]*Department of Chemistry and the Oden Institute for Computational Engineering and Science, The University of Texas at Austin, Austin, Texas 78712-1224, USA*

† Electronic supplementary information (ESI) available. See https://doi.org/10.1039/d2ta02234f

‡ These authors contributed equally to this work.

Dr Won-Hee Ryu received his BS (2006) from the Department of Metallurgical Engineering at Yonsei University, Korea and MS (2007) & PhD (2012) from the Department of Materials Science and Engineering at Korea Advanced Institute of Science and Technology (KAIST), Korea. During his PhD course, he worked as a visiting researcher in the electrochemical energy storage department at the Argonne National Laboratory, USA. Dr Ryu did postdoctoral studies at KAIST (2012–2013) with professor Il-Doo Kim and Yale University (2013–2016) with professor André D. Taylor. He joined the faculty of the Department of Chemical and Biological Engineering at Sookmyung Women's University (Seoul, Korea) as an assistant professor (2016) and is currently working as an associate professor from 2021. His researche studies focus on the development of functional materials and systems for electrochemical energy storage and conversion.

Introduction

Carbon negativity, defined as the net reduction of greenhouse gases (*e.g.* CO_2), has become the most important task for mitigating severe global warming and climate change issues.[1] Considering the impracticability of a sudden prohibition of fossil fuel utilization, alternative solutions to reduce the evolution of CO_2 have been suggested, including post-cleaning treatment strategies such as carbon capture and storage (CCS).[2] Conventional and chemical CCS based on amine-based absorbents have been utilized previously.[3] However, the limitation of current CCS technologies is that scaling them up is energy- and cost-intensive.[4] Electrochemical CCS has been considered as an alternative strategy for capturing the evolved CO_2 and subsequently transforming it into valuable C1- or C2-based products (*e.g.* formic acid, formaldehyde and carbon monoxide) in aqueous solution reservoirs.[5–7] However, this process is non-spontaneous and its voltaic operation (V_{cell} = −1.84 V) consumes electricity or other forms of energy that are generally acquired from fossil fuel-based thermal power generation.[8,9]

Lithium-carbon dioxide (Li–CO_2) batteries, capable of simultaneous energy storage and environmental CO_2 fixation, have recently been spotlighted as promising electrochemical CCS candidates.[10–13] In non-aqueous Li–CO_2 cells, CO_2 reduction ($4Li^+ + 3CO_2 + 4e^- \rightarrow 2Li_2CO_3 + C$, −0.24 V_{SHE}) occurs in combination with the anodic counter reaction of Li ($Li \rightarrow Li^+ + e^-$, −3.04 V_{SHE}) during spontaneous galvanic discharge.[13] In addition, Li–CO_2 cells can be reversibly operated as rechargeable batteries having a high cell voltage (~2.8 V) and theoretical specific energy density (1876 W h kg^{-1}).[14] Therefore, realizing Li–CO_2 batteries would enable the simultaneous capture of CO_2 to reduce CO_2 accumulation and the generation of electricity for energy conversion and storage.[15,16] The reversible electrochemical reaction between Li^+ and CO_2 involves the formation and decomposition of solid lithium carbonate (Li_2CO_3) on the cathode. However, the slow kinetics of the decomposition of Li_2CO_3 (which is an insulator), which is necessary for recharging the battery, frequently causes a large overpotential in the Li–CO_2 cell and consequently reduces the lifespan of the battery.[13]

To overcome this shortcoming, highly active catalysts need to be introduced into the cathodes of Li–CO_2 cells. Multiple studies have examined the feasibility of various noble or non-noble metal-based catalysts loaded on carbon-based supports.[17–25] Although non-noble metal-based catalysts employ abundant and cost-effective materials, their catalytic activity remains inferior to that of noble-metal catalysts.[26–29] The mass of precious metal catalysts loaded on electrodes needs to be reduced without incurring a commensurate loss in catalytic activity.[30,31]

An effective strategy for overcoming the inverse relationship between the loading and activity of noble-metal catalysts is to

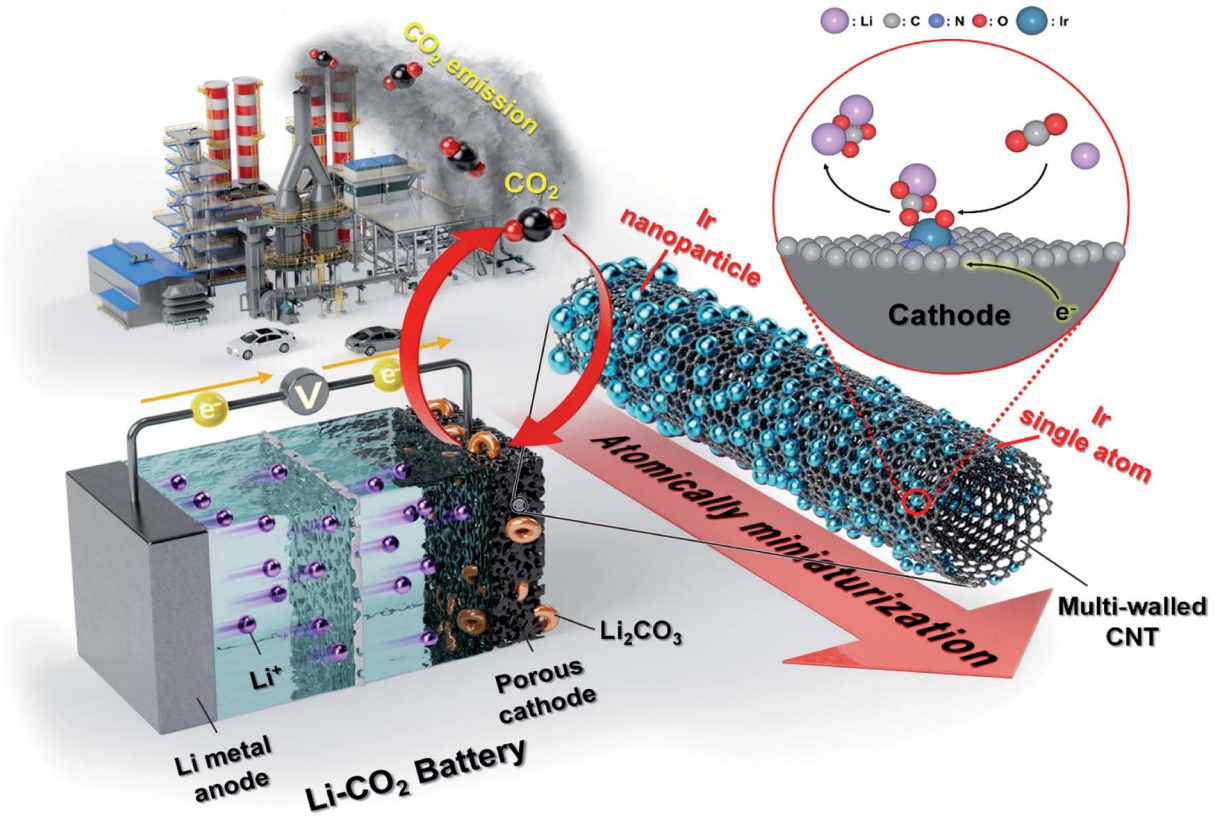

Fig. 1 Schematic illustration of the Li–CO_2 battery employing atomically minimized IrO_x/Ir bi-phase catalysts and the mechanism through which they catalyze the Li–CO_2 reaction.

downsize the catalyst size to ≤1 nm, and eventually to the atomic level, resulting in single-atom catalysts (SACs). This strategy has recently been considered in electrocatalytic studies. SACs are certain to outperform current Li–CO_2 catalysts because of (i) minimized utilization of precious metals, (ii) maximized surface area and the facilitation of numerous reactions on the increased number of dangling bonds present on atomically formed catalysts, (iii) low coordination number and the resulting increase in adsorption capacity for reactants on the surface, (iv) high catalytic activity and homogeneous distribution of catalytic active sites, and (v) increased specific capacity and energy density of the cathode electrode resulting from the minimization of the heavy-metal content.[32–36] Although a few sub-nanometer sized catalysts have been utilized in the cathodes of Li–CO_2 cells, the technique for the reduction of catalyst particle size to prepare SACs needs to be optimized by further understanding the effects of catalyst size and loading effects on the properties of Li–CO_2 cells.[18–25,37,38] While metallic substances such as Fe, Cr, Mn, Co, Ni, and Cu for SACs have been recently applied to Li–CO_2 battery research and showed improved cell performance, further detailed studies regarding catalyst size effects are needed.[39,40]

In this study, we attempted to atomically miniaturize Ir, which is known to be an effective CO_2 evolving catalyst, on highly conductive N-doped carbon nanotubes (NCNTs) to create efficient cathode catalysts for Li–CO_2 cells (Fig. 1). To prove the effectiveness of IrO_x/Ir SACs in Li–CO_2 cells, we controlled the particle size and loading of Ir catalysts on the NCNTs. As the size of the Ir particles was reduced, the abundance of defects on the particles increased, and the defects existed in the form of Ir^{4+} oxide at the minimum catalyst particle size. The nitrogen groups on the CNTs functioned as artificial defects, providing strong adsorption and preferred nucleation sites for IrO_x/Ir SACs as well as increasing the electron conductivity *via* the formation of unpaired electrons. The nucleation and growth characteristics of IrO_x/Ir SACs on NCNTs were elucidated in detail using first-principles calculations and material characterization. The IrO_x/Ir SAC-loaded NCNTs (s-Ir/NCNTs) was evaluated as a cathode catalyst for Li–CO_2 cells, and its electrochemical performance was compared to that of a larger-sized catalyst and higher dosages of Ir on NCNTs, denoted as m-Ir/NCNTs and l-Ir/NCNTs, respectively. Furthermore, the binding energies of the Ir catalytic site were evaluated to establish a probable mechanism for the Li–CO_2 reaction pathway. We expect that the strategy of atomically miniaturizing precious catalyst materials on cathode substrates will maximize the activation effect and realize a significant breakthrough in the electrochemical performance of Li–CO_2 cells while minimizing the cost of the catalyst.

Experimental

Materials

Smw100 (SouthWest NanoTechnologies Inc., Specialty Multi-Wall (SMW) carbon nanotubes (CNTs)), melamine ($C_3H_6N_6$, 99%), and hydrogen hexachloroiridate(IV) hydrate ($H_2IrCl_6 \cdot xH_2O$, 36.0–44.0% Ir basis) were purchased from Sigma-Aldrich (Korea). Tetraethylene glycol dimethyl ether (TEGDME, 99%), *bis*(trifluoromethane)sulfonimide lithium salt (LiTFSI, 99.95%), poly(vinylidene fluoride) (PVdF, $M_w \approx$ 180 000), and *N*-methyl-2-pyrrolidone (NMP, anhydrous, 99.5%) were purchased from Sigma-Aldrich (Korea). Residual moisture was removed from TEGDME by immersing freshly activated molecular sieves (4 Å) in the solvent for two weeks.

Synthesis of Ir catalysts loaded on N-doped CNTs

Ir particles loaded onto N-doped CNTs (Ir-NCNTs) were synthesized by filtration of a dispersed precursor solution and subsequent thermal treatment. Initially, specialty multi-wall carbon nanotubes (SMWCNTs) and melamine were homogeneously mixed in a mass ratio of 1 : 1.3 using a mortar. The mixed powder was immediately calcined in a tube furnace at 600 °C in a flow of N_2 gas for 1 h at a heating rate of 10 °C min^{-1}. This completed the synthesis of the N-doped CNTs. In the following step, 0.05 g of the as-synthesized NCNTs and 0.0165 g H_2IrCl_6 were dispersed in 25 and 12.5 mL of EtOH, respectively, and sonicated for 20 min. The dispersed NCNTs and H_2IrCl_6 solutions were subsequently mixed and sonicated for 30 min to obtain s-Ir/NCNTs. Subsequently, the mixed solution was filtered under reduced pressure and washed several times using EtOH/DI water. The retentate was calcined in a tube furnace at 600 °C for 1 h in an Ar atmosphere at a heating rate of 10 °C min^{-1}. As in the previous process, m-Ir/NCNT and l-Ir/NCNT samples were synthesized using 0.05 g and 0.1 g of H_2IrCl_6, respectively.

Characterization

The percentage by weight of Ir loaded on the NCNTs was investigated by thermogravimetric analysis (TGA, TGA4000, PerkinElmer) performed at a heating rate of 10 °C min^{-1} in a flow of air. The surface morphologies of the catalyst samples were observed by scanning electron microscopy (SEM, S-4300SE, Hitachi) and transmission electron microscopy (TEM, JEM-2100F, Cs corrector, JEOL/CEOS), and their elemental compositions were determined by energy-dispersive X-ray spectroscopy (EDS). The crystallinity and degree of agglomeration were characterized by X-ray diffraction (XRD, Ultima IV, Rigaku) analysis. The characterization of the bonds, including the identification of the elements on the surface and their oxidation numbers, was performed using X-ray photoelectron spectroscopy (XPS, K-alpha, Thermo Scientific, UK).

Preparation of Li–CO_2 cells

The oxygen electrode was fabricated using nitrogen-doped multiwalled carbon nanotubes (MWCNTs; 90 wt%) and PVdF (10 wt%) dissolved in NMP. The slurry was pasted onto a ∅12 mm gas diffusion layer (GDL) current collector and was dried for 4 h at 40 °C in a vacuum. The average slurry mass loading was 0.4 mg per ∅ 12 mm GDL. The electrolyte was prepared by dissolving LiTFSI in TEGDME (1 M) and stirring for 24 h at room temperature. ∅ 12 mm Li-metal foil was used as the anode and a glass fiber (Whatman GF/A microfiber filter paper) was used as the separator. Coin cells containing several

holes were used for cycling tests, EIS, and DEMS. All the cells were assembled in an Ar-filled glove box. The cells were purged with CO_2 (99.999%) prior to testing.

Electrochemical characterization

Charge–discharge testing of iridium loaded Li–CO_2 cells was performed using a potentiostat/galvanostat (WonATech, Co., Ltd., WBCS3000, Korea) at 50 mA g^{-1} in a range of 2.3–4.5 V *versus* Li/Li^+. For the cycling tests, a potentiostat/galvanostat (WonATech, Co., Ltd., WBCS3000L, Korea) was operated at 50 mA g^{-1} with a limited capacity of 500 mA h g^{-1} in the same voltage range as maintained in the charging–discharging tests. Prior to the electrochemical tests, the cells were purged with CO_2 gas and the tests were performed at room temperature.

Ex situ characterization

The crystal structures and electrode surface characteristics after cycling were analyzed using X-ray diffraction (XRD, Ultima IV, Rigaku), Fourier-transform infrared (FT-IR) spectroscopy, and Raman spectrometry (LabRam Aramis, Horiba Jobin Yvon). The samples were prepared by galvanostatically discharging and charging at 50 mA g^{-1} carbon. The electrode was collected after discharging (1^{st} cycle) and after charging (1^{st} cycle). A pristine electrode was prepared to compare each sample. The cells were disassembled in an Ar-filled glove box after discharging and charging. The collected electrodes were sealed to prevent surface-oxidation during transfer and measurement.

In situ differential electrochemical mass spectroscopy

Mass spectroscopy (Hiden Analytical, UK) was used to quantify the amount of CO_2 evolved during the electrochemical tests. Coin cells having a hole in the case were used for the DEMS test and inserted into a DEMS cell, enabling gas to flow in and out of them. Each cell was connected to the DEMS analysis line, which was comprised of a mass flow controller, a gas inlet/outlet line for cell connection, and a mass spectrometer. Ar gas (99.999%) supplied at 15 mL min^{-1} was used as the carrier. The interior of the cell was washed using Ar to remove residual impurities, whereafter the cell was discharged at a constant current density of 100 μA in a voltage range of 2.0–4.5 V.

Computational details

Generalized gradient approximation (GGA)-level spin-polarized density functional theory (DFT) calculations were performed with the Vienna *ab initio* simulation package (VASP) using a plane-wave basis set with a cut-off energy of 400 eV. The revised Perdew–Burke–Ernzerhof (RPBE) functional was used to describe the electron exchange and correlation.[41–43] The van der Waals interaction was considered by employing the DFT-D3 dispersion correction developed by Grimme.[44,45] The Brillouin zone was sampled at 4 × 4 × 1 using the Monkhorst–Pack scheme. The convergence criteria for the electronic and geometric optimizations were set at 10^{-5} eV and 10^{-2} eV $Å^{-1}$, respectively.

In this study, we prepared four Ir systems with different particle sizes, supported on NCNTs, and the surface slab model. The smallest particle size was exhibited by the IrO_2 single-atom catalyst (SAC) surrounded by four N atoms on the graphene layer. The Ir_6 and Ir_{12} NPs supported on the NCNTs had a (111) surface motif to form close-packed NPs and minimize the surface energy to obtain a stable NP structure. We also constructed a simple Ir (111) slab model having four atomic layers to compare the catalytic activities. All the systems had a 20 Å vacuum gap in the *z*-direction; the two bottom-most Ir atomic layers of the Ir (111) surface were fixed in their bulk positions.

To calculate the rates of the CO_2 reduction and evolution reactions (CRR and CER, or discharging and charging, respectively) occurring in a Li–CO_2 battery, the following reaction steps and adsorbates were considered.[46–49]

$$\Delta G_1 = * + CO_2(g) \rightarrow CO_2^* \quad (1)$$

$$\Delta G_2 = CO_2(g) + CO_2^* \rightarrow C_2O_4^* \quad (2)$$

$$\Delta G_3 = CO_2^* + (Li^+ + e^-) \rightarrow LiCO_2^* \quad (3)$$

$$\Delta G_4 = * + (Li^+ + e^-) \rightarrow Li^* \quad (4)$$

$$\Delta G_5 = Li^* + CO_2(g) \rightarrow LiCO_2^* \quad (5)$$

$$\Delta G_6 = * + CO_2(g) + (Li^+ + e^-) \rightarrow LiCO_2^* \quad (6)$$

$$\Delta G_7 = LiCO_2^* + CO_2(g) \rightarrow LiC_2O_4^* \quad (7)$$

$$\Delta G_8 = C_2O_4^* + (Li^+ + e^-) \rightarrow LiC_2O_4^* \quad (8)$$

$$\Delta G_9 = LiCO_2^* + (Li^+ + e^-) \rightarrow Li_2CO_2^* \quad (9)$$

$$\Delta G_{10} = Li_2CO_2^* + CO_2(g) \rightarrow Li_2C_2O_4^* \quad (10)$$

$$\Delta G_{11} = LiCO_2^* + CO_2(g) + (Li^+ + e^-) \rightarrow Li_2C_2O_4^* \quad (11)$$

$$\Delta G_{12} = LiC_2O_4^* + (Li^+ + e^-) \rightarrow Li_2C_2O_4^* \quad (12)$$

$$\Delta G_{13} = Li_2C_2O_4^* + LiCO_2^* + (Li^+ + e^-) \rightarrow 2(Li_2CO_3)^* + C^* \quad (13)$$

$$\Delta G_{14} = Li_2C_2O_4^* + Li_2CO_2^* \rightarrow 2(Li_2CO_3)^* + C^* \quad (14)$$

The discharging (U_{DC}) and charging (U_C) potentials were calculated from the reaction energy diagram drawn using the following equation.[50,51]

$$\Delta G(U) = \Delta E + \Delta ZPE - T\Delta S + neU \quad (15)$$

where ΔE is the reaction energy obtained from the DFT calculations, ΔZPE is the zero-point energy correction, ΔS is the change in entropy, and U is the applied potential. The chemical potential of the lithium cation and electron pair ($Li^+ + e^-$) at

standard temperature and pressure (STP) was calculated to be $\mu^0_{Li(s)} - eU$ by assuming equilibrium at the electrode potential of lithium (0 V *vs.* Li/Li^+).[52–54] We calculated the equilibrium potential of the CRR and CER based on the aforementioned assumption to be 2.695 V (*vs.* Li/Li^+), and it was experimentally determined to be 2.8 V (*vs.* Li/Li^+).[13] A discrepancy of approximately 0.1 V remains between the experimental and simulated results, which is considered to be negligible, because the critical parameter determining the performance of Li–CO_2 batteries is the potential gap between the discharging and charging reactions.

Results and discussion

The morphological characteristics of atomically minimized Ir particles loaded on NCNTs were investigated by TEM, and the resulting micrographs are shown in Fig. 2a–h. The NCNTs had multiple walls and an average diameter of 17.3 nm (Fig. 2a). Although the NCNTs and Ir-loaded NCNTs appeared to be morphologically similar in the low-magnification SEM images, the Ir particles were observed to be decorated as circular shapes on the surfaces of the NCNTs (Fig. 1 and S1†). To confirm the differences between the Ir particles in s-, m-, and l-Ir/NCNTs,

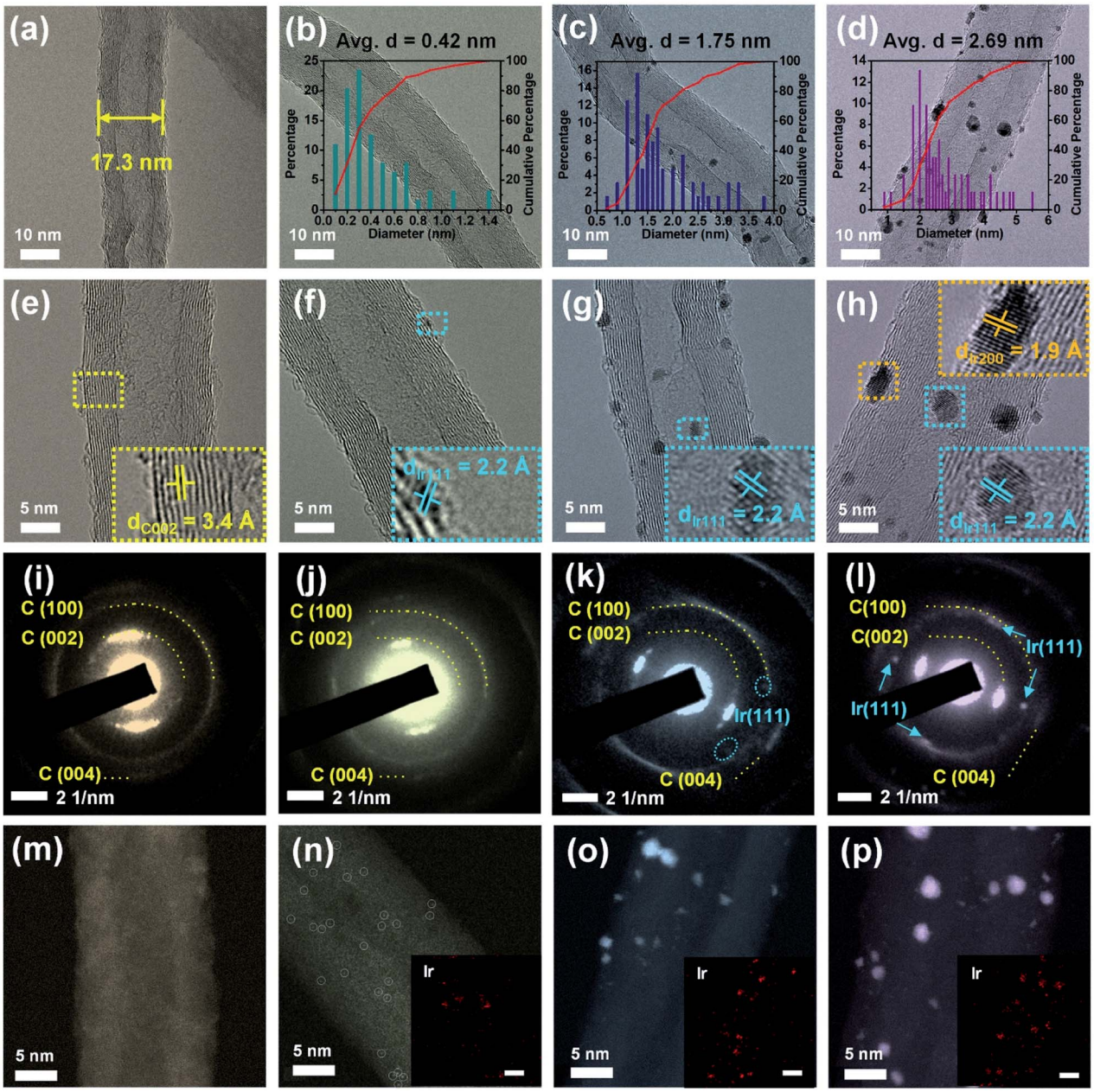

Fig. 2 Morphological characterization of NCNTs (a, e, i and m); s-Ir/NCNTs (b, f, j and n); m-Ir/NCNTs (c, g, k and o) and l-Ir/NCNTs (d, h, l and p): (a–h) TEM images, (i–l) SAED patterns, (m–p) STEM images and (insets of n–p) EDS elemental maps. The insets of Fig. 2b–d demonstrate the relatively uniform Ir particle distribution of each sample.

the particle size distributions (calculated using digital micrography software) were plotted and shown in the insets of Fig. 2b–d. The observable size distribution of Ir particles was 0.1–1.4, 0.7–3.8, and 0.9–5.5 nm for s-Ir/NCNTs, m-Ir/NCNTs, and l-Ir/NCNTs, with averages of 0.42, 1.75 and 2.69 nm, respectively. The plots of cumulative percentage are roughly single-stair-shaped for all Ir/NCNT samples, which indicates relatively uniform distributions of Ir particles in each sample (insets of Fig. 2b–d). In particular, the slope of the cumulative percentage plot for s-Ir/NCNTs appeared to be steeper than those for m- and l-Ir/NCNTs, indicating that smaller Ir particles were uniformly loaded on the NCNTs (Fig. S2†). Furthermore, the modes of the particle size distribution for s-, m-, and l-Ir/NCNTs were 0.3, 1.3, and 2 nm, exhibiting fractions of 23.44, 15.63, and 13.11%, respectively. This observation further proves that the atomically minimized Ir particles have a more consistent particle size distribution. The amount of atomically minimized Ir particles loaded on the NCNTs was quantitatively evaluated by thermogravimetric analysis (TGA) (Fig. S3†). To investigate the thermal decomposition behavior of the Ir catalyst-loaded NCNTs, the samples were calcined in a temperature range of 30–800 °C at a heating rate of 10 °C min^{-1} in air.

Significant weight losses occurred between 400 and 600 °C for all samples, corresponding to the decomposition of carbon nanotubes into CO_2 *via* reaction with O_2. The residual weight percentages at 800 °C were 3.2, 8.8 and 16.7% for s-, m-, and l-Ir/NCNTs, respectively, indicating that the mass of residual Ir species was reduced because the size of the Ir particles was effectively controlled by altering the amount and concentration of the Ir precursor.

Enlarged images of the lattice fringes of the NCNTs and Ir/NCNT materials are presented in Fig. 2e–h for a closer examination of the crystalline and morphological features. The (002) plane of the CNT walls corresponding to 3.4 Å (annotated in yellow) was observed for all the samples, and the (111) planes of the Ir phase corresponding to 2.2 Å (annotated in blue) were observed for all Ir/NCNTs. The (200) plane of the Ir phase corresponding to 1.9 Å (orange) was additionally detected in l-Ir/NCNTs, and is attributed to further crystallization and particle growth of the Ir catalysts.

The selected area electron diffraction (SAED) patterns were also assigned to the C and Ir planes as shown in Fig. 2i–l. The (002), (100), and (004) planes of the carbon components were observed in the form of typical polycrystalline ring patterns for all samples. Following the anchoring of the Ir catalysts, single crystalline spot patterns attributed to the Ir (111) plane were exhibited by both m-and l-Ir/NCNTs, which agrees closely with the reference data (JCPDS 046-1044).[55]

High-angle annular dark-field scanning transmission electron microscopy (HAADF-STEM) images were captured to specifically identify the IrO_x/Ir SACs and nanoparticles (NPs) as bright circles in Fig. 2n–p. Agglomerated Ir NPs were more common in l-Ir/NCNTs than in s- and m-Ir/NCNTs. In contrast, the Ir particles indicated by the empty circles in Fig. 2n are uniformly distributed with small dots, indicating a uniform atomic distribution of the Ir catalysts instead of nanoscale particles. The STEM and EDS mapping images (Fig. S4a–c†) of the NCNT materials confirmed the existence of N dopants in CNTs, which provide nucleation sites for Ir and enhance the electron-conductivity. While Ir particles were distributed in a manner closely resembling that in SACs with few agglomerated nanoparticles in the s-Ir/NCNTs, the Ir particles in m- and l-Ir/NCNTs were further aggregated (Fig. S4d–f†).

X-ray diffraction (XRD) and X-ray photoelectron spectroscopy (XPS) experiments were conducted to investigate the crystalline and surface structures of the Ir/NCNT materials having different mean sizes of Ir particles (Fig. 3). The XRD patterns are shown in Fig. 3a. The patterns of all the samples exhibited typical peaks at 26° and 43°, corresponding to the C (002) and C (100) planes (JCPDS card no. 15-0870), respectively.[26] The peak of Ir (111) at 41° gradually increased with increasing Ir content for m-Ir/NCNTs and l-Ir/NCNTs. In the case of l-Ir/NCNTs, the peak for Ir (111) became dominant instead of that of C (002), and additional peaks attributable to Ir (200) and Ir (220) appeared at 47° and 69°, respectively, because of the formation of significant numbers of aggregated Ir metal nanoparticles.[55] There was no significant difference between NCNTs and s-Ir/NCNTs, demonstrating that the Ir catalysts were atomically dispersed on NCNTs for s-Ir/NCNTs without significant particle segregation and crystallization.

The XPS results were used to identify the existence of each atomic element (C, N, and Ir) and its chemical state in the Ir/NCNT materials. The C 1s, N 1s, and Ir 4f XPS spectra are shown in Fig. 3b–d. In the C 1s spectra, peaks attributed to C–C, C–N, C–O, C=O, and C–H bonds appeared for all samples at 284.8, 285.7, 286.6, 288, and 283.93 eV, respectively (Fig. 3b).[56–59] This result indicates that the structure of the NCNT scaffolds is consistent among the samples without any contamination or structural change caused by the Ir-loading process. The C–N and $C–N^+$ peaks at 399.5 and 401.5 eV in the N 1s spectra imply that the N-doping of the CNTs was successful for all the samples (Fig. 3c).[60] Nitrogen doped into CNTs improves the electronic conductivity of the carbonaceous material owing to the generation of unpaired electrons.[61–64] In this study, the N sites also provided energetically preferable nucleation sites to stably load IrO_x/Ir SACs onto the CNT backbone. The existence and structural information of IrO_x/Ir SACs on NCNTs were confirmed by examining the Ir 4f spectra (Fig. 3d). The Ir^{4+}/Ir^0 ratio was also monitored to confirm the formation of the IrO_2 phase on IrO_x/Ir SACs, which is associated with the coordination of oxygen with the dangling bonds of atomically distributed Ir catalysts having low coordination numbers. The peaks at 63.8 and 60.8 eV are associated with Ir $4f_{5/2}$ and Ir $4f_{7/2}$ of the metallic Ir^0 phase, respectively. In contrast, the peaks at 65 and 62 eV correspond to Ir $4f_{5/2}$ and Ir $4f_{7/2}$ of the Ir^{4+} phase (IrO_2), respectively.[65–67] The relative intensities of the Ir^0 peaks to the Ir^{4+} peaks, indicating the binding energy of the Ir particles, are shown and summarized in Table S1† and Fig. 3d. The height ratios of Ir^{4+} peaks to Ir^0 peaks were 51.9, 37.7 and 26.2% while the area ratios were 71.9, 54.2 and 25% for s-, m-, and l-Ir/NCNTs, respectively. While the metallic phase related to the Ir^0 peaks was dominant for all samples, the percentage of Ir^{4+} (which is associated with the IrO_2 phase) exhibited an increasing tendency with the decreasing Ir content on the NCNTs (l-Ir/

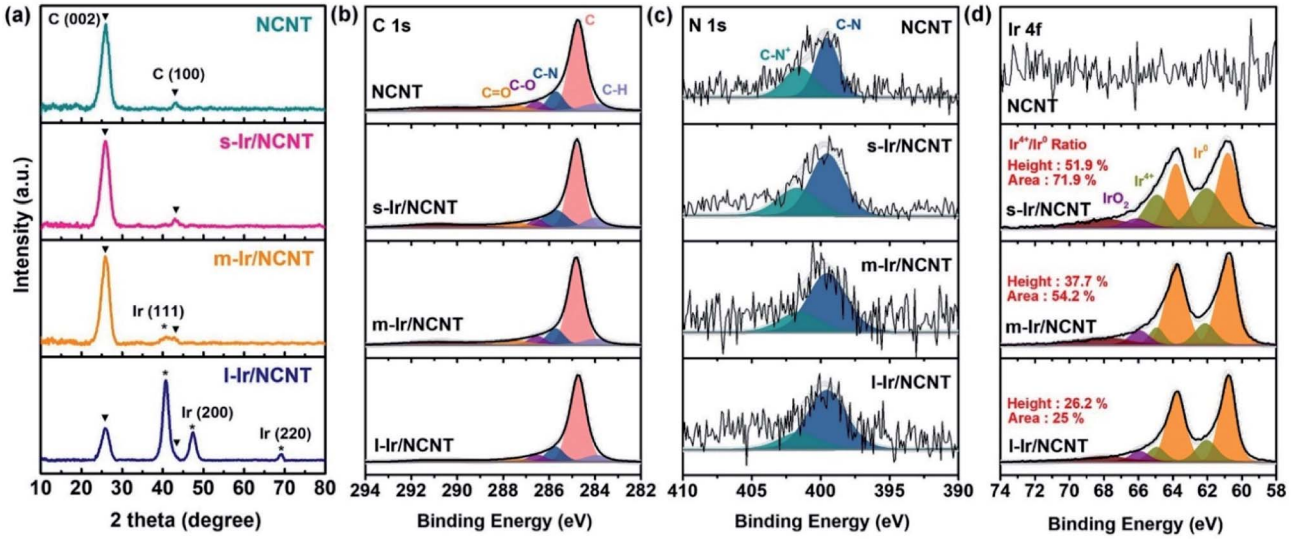

Fig. 3 Structural and chemical characterization of NCNTs and s-, m- and l-Ir/NCNTs: (a) XRD patterns; (b) C 1s, (c) N 1s, and (d) Ir 4f XPS spectra.

NCNTs → s-Ir/NCNTs). This distinct tendency verifies that the dangling bonds on the Ir surface readily adsorb oxygen species to reduce and stabilize the surface energy. The coordination number of Ir was the lowest in the case of s-Ir/NCNTs, implying that further defects were formed in the IrO_x/Ir bi-phase. The low coordination number and surface oxygen density of IrO_x/Ir SACs allow facile adsorption of Li^+ and CO_2 reactants, and consequently, improve the catalytic activity for the Li–CO_2 reaction.[36].

To further validate the size effect of the Ir catalyst in Li–CO_2 cells, we simulated four different systems, including s-, m-, and l-Ir/NCNTs, and one slab model for this simulation study. For the s-Ir/NCNT system, we fabricated a typical IrN_4 SAC on the graphene layer,[68–70] and placed two O atoms at the Ir atom to represent the IrO_2 SAC, as confirmed by the XPS results for high ratios of Ir^{4+}/Ir^0 (Fig. 4a). For the m-Ir NPs system, we created larger numbers of C-vacancies terminated by eight N atoms

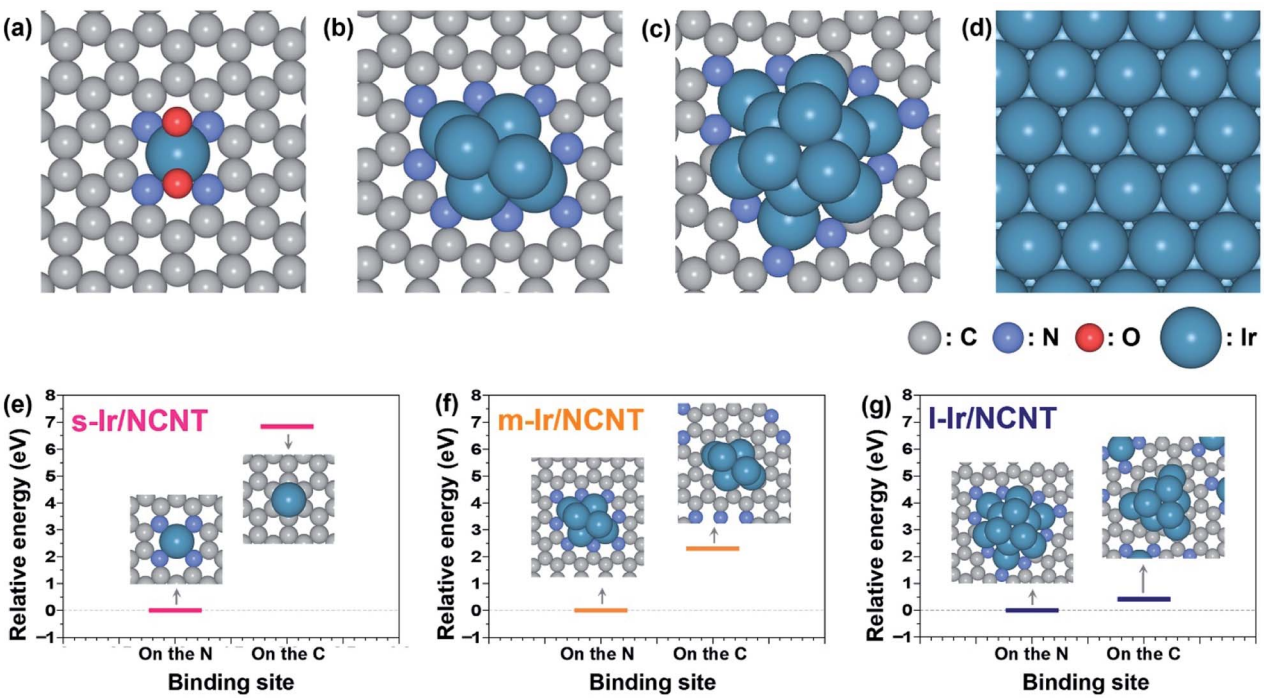

Fig. 4 Illustrations of structures representing the s-, m, and l-Ir particles on the NCNT: (a) IrO_2 SAC for small particles, (b) Ir_6 NP for medium-sized particles, (c) Ir_{12} NP for large NPs, and (d) Ir (111) surface for comparison. Relative binding energies of (e) Ir atom, (f) Ir_6, and (g) Ir_{12} NP on the NCNTs.

than for the IrO_2 SAC (Fig. S5a and b†), and we placed the Ir_6 NP exactly above the vacancies (Fig. 4b). For the l-Ir NP system, Ir_{12} NPs were supported on the NCNTs, similarly to m-Ir NPs (Fig. 4c). When we created the m- and l-Ir NPs on the NCNTs, we attempted to minimize the surface energy by arranging Ir atoms solely with the (111) surface motif. Finally, we constructed a simple Ir (111) surface slab model for comparison (Fig. 4d).

We introduced N doping into the CNT backbones to facilitate the adsorption and nucleation of the Ir catalysts. After preparing the Ir particle systems, we compared the relative stability of Ir particles on different binding sites on N or C atoms. Initially, we calculated the binding energies of Ir particles (eV/Ir atom) above the N atom and assumed them to be the baselines (0 eV/Ir atom). Similarly, we calculated the binding energies of Ir particles on the C atom, and the results are presented in Fig. 4e–g. The s-, m-, and l-Ir particles on the C atom exhibited positive (*i.e.*, unstable) binding energies of 6.842, 2.315, and 0.413 eV/Ir atom, respectively. In other words, Ir atoms or NPs were anchored near the N atoms. Therefore, we created rational s-, m-, and l-Ir particle models on the NCNTs and found that all the Ir particles were favorably positioned near the N atoms.

To verify the catalytic efficiency of IrO_x/Ir bi-phase SACs, we performed electrochemical tests using Li–CO_2 cells employing Ir-loaded NCNTs having different catalyst sizes (Fig. 5). The discharge/charge profiles of the Li–CO_2 cells containing Ir catalysts of different particle size ranges are illustrated in Fig. 5a–c. The magnitude of the catalytic effect depended strongly on the size of the catalyst particles. The l-Ir/NCNTs having the largest Ir particles exhibited more polarized discharge/charge profiles than the s-Ir/NCNT and m-Ir/NCNT catalysts, and the overpotential of the charge/discharge profiles increased as cycling continued. l-Ir/NCNTs deteriorated rapidly after 20 cycles and exhibited an unstable tendency in the CER region as the charge voltage approached the upper limit of the voltage window (4.5 V) before the charge reaction was completed. In the discharge region, the voltage plateau gradually decreased between the 15th and 20th cycles, whereafter it decreased rapidly to the lower limit of the voltage window (2.35 V). In contrast, the s-Ir/NCNTs and m-Ir/NCNTs exhibited significantly lower CER overpotentials of 3.3 V and 3.4 V, respectively, after the 20th cycle. The performance of the Li–CO_2 cell employing m-Ir/NCNTs decreased slightly until 80 cycles in the discharge region. In contrast, the loss in

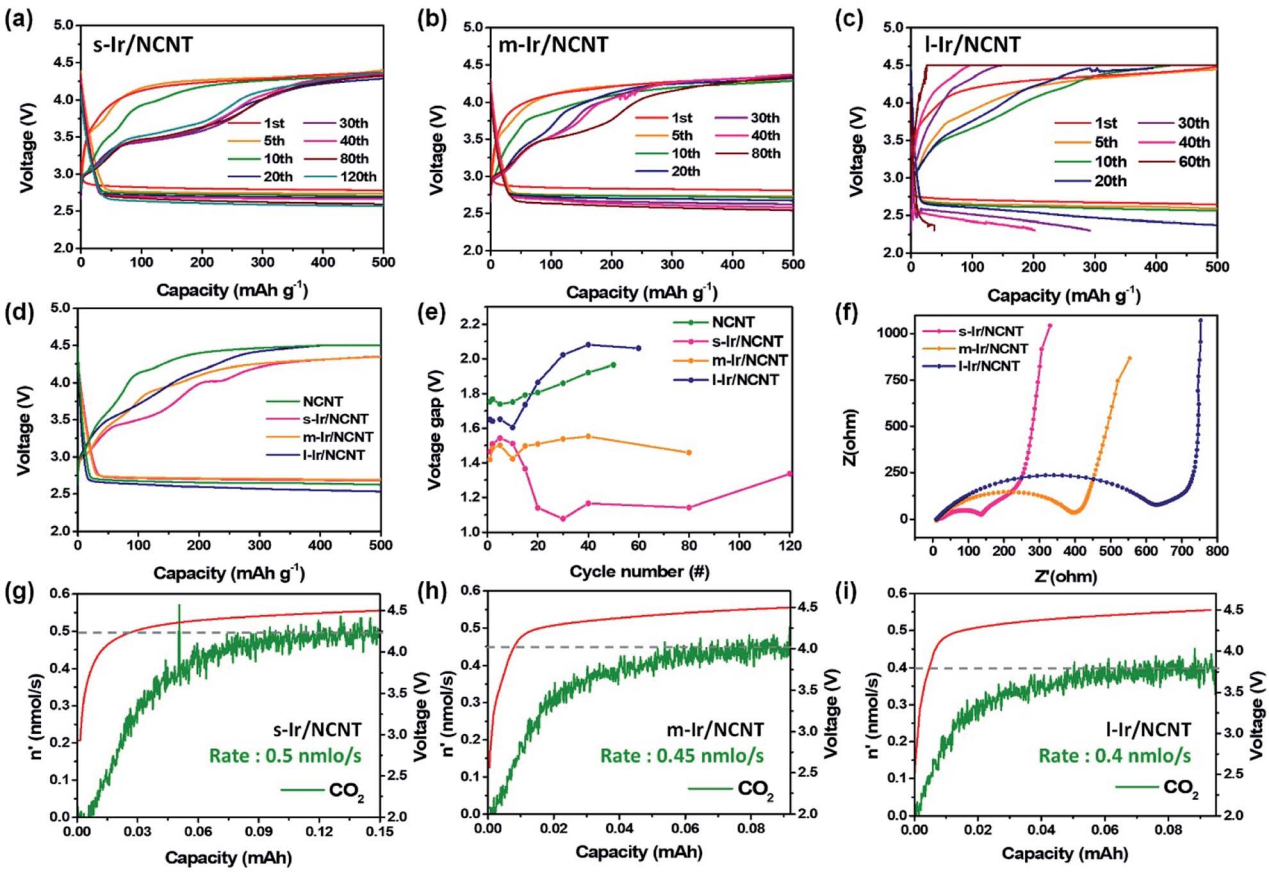

Fig. 5 Electrochemical cell data of NCNTs and s-, m- and l-Ir/NCNTs: (a–c) cycling performance of Li–CO_2 cells fabricated using s-, m-, and l-Ir/NCNTs loaded electrodes measure at 50 mA g_{carbon}^{-1} with a limited capacity of 500 mA h g_{carbon}^{-1}. (d) Discharge/charge curves during the 15th cycle. (e) Voltage gap graphs calculated during the discharge and charge reactions for Li–CO_2 cells at 250 mA h g^{-1} during each cycle. (f) EIS profiles of the s-, m- and l-Ir/NCNT-containing electrode after 10 cycles. (g–i) *in situ* DEMS results of the gas evolution rate for CO_2 during charging in cells with s-, m- and l-Ir/NCNTs.

performance was negligible for the cell employing s-Ir/NCNTs even until the 120th cycle. In summary, the catalytic effect of s-Ir/NCNTs was superior to that of m-Ir/NCNTs and l-Ir/NCNTs. This suggests that the smaller the particle size on the atomic scale, the higher the catalytic activity and the greater the cyclability of the Li–CO_2 reaction. As shown in Fig. 3d and Table S1,† the fraction of Ir^{4+} (corresponding to IrO_2) is relatively high and more dangling bonds are observed in s-Ir NCNTs, and the ionic conductivity and catalytic adsorption behavior with Li^+ and CO_2 as the reactants are superior to those of Ir^0. The charge/discharge profile of the 15th cycle is presented for further inspection of the electrochemical characteristics of the as-fabricated Li–CO_2 batteries loaded with Ir particles of different sizes (Fig. 5d). In all cases where the Ir catalyst was loaded, significantly higher catalytic effects were observed in the CO_2 reduction reaction (CRR) and CO_2 evolution reaction (CER) regions than for the pristine NCNT reference lacking the Ir catalyst, which verifies the catalytic effect of the Ir components (Fig. 5d and S6†). The s-Ir/NCNT-loaded Li–CO_2 cell exhibited excellent performance with the lowest overpotential among all the cells.

Fig. 5e shows the voltage gaps of Ir catalysts of different particle sizes collected and calculated in the middle of the discharge and charge reactions (at 250 mA h g^{-1}) of each cycle. The Li–CO_2 cells employing smaller-sized Ir particles exhibited lower voltage gaps in the discharge/charge curves than the pristine Li–CO_2 cells lacking a catalyst. Although l-Ir/NCNTs exhibit a catalytic effect during the initial cycles, the voltage gap increases gradually after the 10th cycle, until eventually, its value is higher than that of the pristine and catalyst-containing cells. The voltage gap of the Li–CO_2 cell employing m-Ir/NCNTs remained below 1.6 V through 40 cycles. However, the Li–CO_2 cells employing IrO_x/Ir SACs loaded on NCNT supports (s-Ir/NCNTs) outperformed the cells employing larger catalysts, exhibiting a significantly lower voltage gap of 1.07 V in the 30th cycle. Interestingly, while the voltage gap of s-Ir/NCNTs was similar to that of m-Ir/NCNTs until 10 cycles, the overpotential of the s-Ir/NCNT-containing cells suddenly decreased from 1.5 V to 1 V. This impressive phenomenon, caused by a sudden activation (and corresponding enhancement in catalytic activity) at the end of a few cycles, demonstrated the superior catalytic performance and effective function of SACs, even when synthesized using small amounts of noble metal catalysts.

The accumulation of insulating discharge products such as Li_2CO_3 on the cathode surface increases the surface resistance.[71] The existence of IrO_x/Ir SACs on the electrode surface can relieve the resistance and facilitate charge transfer at the electrochemical interface.

To measure the surface resistance of Li–CO_2 cells employing different Ir catalysts, we present the electrochemical impedance spectroscopy (EIS) profiles recorded after 10 cycles (Fig. 5f). The diameter of the semicircle in the Nyquist plot at high frequencies corresponds to the magnitude of the charge-transfer resistance at the electrode/electrolyte surface.[72] The s-Ir/NCNT catalysts (~150 Ω) exhibited a significantly lower charge transfer resistance than the m-Ir/NCNT (~400 Ω) and l-Ir/NCNT (~650 Ω) catalysts. The charge-transfer resistance of s-Ir/NCNTs was one-fourth that of l-Ir/NCNTs. These results verified that the reversible formation and decomposition of Li_2CO_3 products were successfully facilitated by the atomically distributed IrO_x/Ir biphase catalysts.

To confirm the enhanced reversibility of the Li–CO_2 cell employing the atomically distributed IrO_x/Ir bi-phase catalysts, *in situ* differential electrochemical mass spectrometry (DEMS) was conducted by monitoring the CO_2 evolution rates of cells employing Ir catalysts of differing particle sizes (Fig. 5g–i and S7†). Considering the Li_2CO_3 decomposition reaction ($2Li_2CO_3 + C \rightarrow 4Li^+ + 3CO_2 + 4e^-$), CO_2 gas should be detected during recharge.[13] The evolution rate of CO_2 using s-Ir/NCNTs (0.5 nmol s^{-1}) at the end of charging owing to the reversible decomposition of Li_2CO_3 products was higher than that using m-Ir/NCNTs (0.45 nmol s^{-1}) and l-Ir/NCNTs (0.4 nmol s^{-1}). This indicates that the reverse-decomposition of Li_2CO_3 can be facilitated by introducing atomically sized catalysts instead of larger particles. The enhanced reversibility of the Li–CO_2 reaction assisted by IrO_x/Ir SACs was confirmed through *ex situ* electrode surface analysis (Fig. S8†). The XRD patterns contained dominant peaks associated with the crystalline Li_2CO_3 phase on the discharged electrode, and the peaks reversibly disappeared as the electrode was recharged. To further examine the chemical structure of the discharge products, we conducted Fourier-transform infrared (FT-IR) spectroscopy of the electrode after charging and discharging, respectively.[73] Peaks near 1420 cm^{-1} related to Li_2CO_3 were observed following discharge and disappeared following recharge, which is consistent with the XRD results. Similar results can also be confirmed from the Raman spectra regarding the reversible formation and decomposition of Li_2CO_3 (1100 cm^{-1}) during discharging and charging.

To elucidate the experimental findings regarding the CRR (discharge) and CER (charge) reaction activities, DFT calculations were performed to determine the operating potential based on the reaction energy diagram. We initially explored all nine possible intermediates for both the CRR and CER: Li*, CO_2^*, $C_2O_4^*$, $LiCO_2^*$, $Li_2CO_2^*$, $LiC_2O_4^*$, $Li_2C_2O_4^*$, $Li_2CO_3^*$, and C*, and 14 different reaction energy steps, represented in eqn (1)–(14) and Fig. S9.† In the case of the CRR, according to the Gibbs free energy changes in Table S2†, irrespective of the system, the binding of CO_2 (g) (ΔG_1) or making $C_2O_4^*$ (ΔG_2) as an initial reaction step was more unstable than the binding of ($Li^+ + e^-$) (ΔG_4) or the direct conversion to $LiCO_2^*$ from ($Li^+ + e^-$) and CO_2 (g) (ΔG_6). Among the three possible intermediates, $LiC_2O_4^*$ (ΔG_7), $Li_2C_2O_4^*$ (ΔG_{11}), and $Li_2CO_2^*$ (ΔG_9) from $LiCO_2^*$, $Li_2CO_2^*$ (ΔG_9), and $Li_2C_2O_4^*$ (ΔG_{11}) could occur naturally ($\Delta G < 0$). However, the conversion from Li_2CO_2 to $Li_2C_2O_4$ (ΔG_{10}) is an endothermic reaction ($\Delta G > 0$), indicating that $LiCO_2$ would preferably convert to $Li_2C_2O_4^*$ (ΔG_{11}) through the Langmuir–Hinshelwood mechanism.[74] Similarly, we checked all the possible reaction pathways and concluded that the most feasible path would be $\Delta G_4 \rightarrow \Delta G_5 \rightarrow \Delta G_{11} \rightarrow \Delta G_4 \rightarrow \Delta G_5 \rightarrow \Delta G_{13}$ (see the red arrow in Fig. S9†), which was also used to calculate the charging (U_C) and discharging (UDC) potentials of the Li–CO_2 battery (Fig. 6). When we calculated the operating potential, we separated the reaction steps into involved and

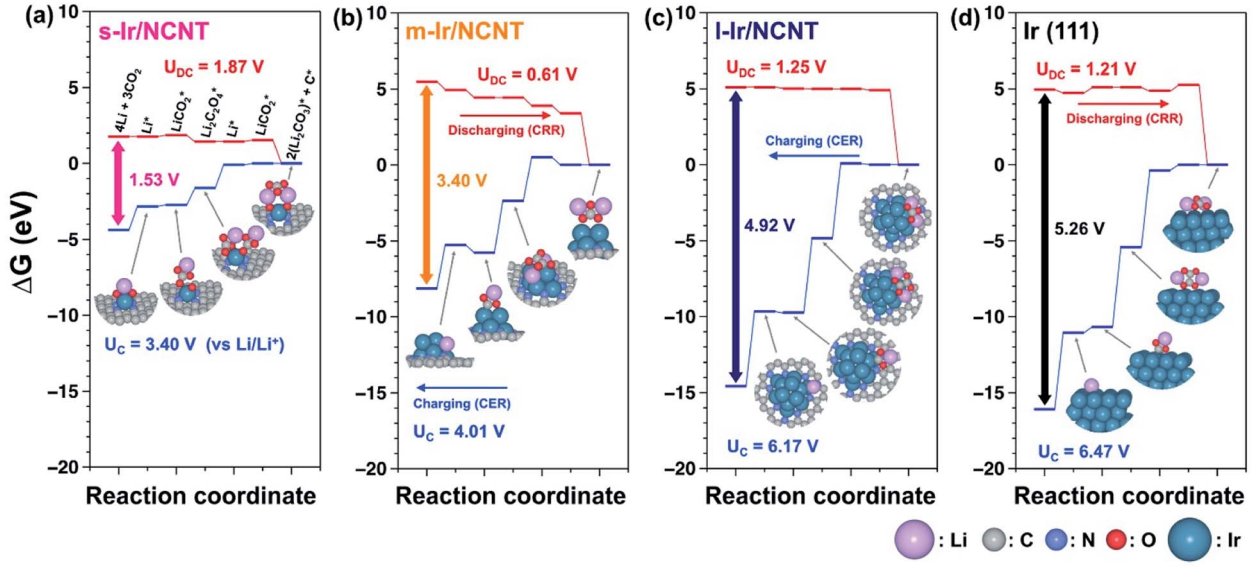

Fig. 6 Reaction energy diagram of charging and discharging for the Li–CO_2 battery on (a) s-Ir/NCNT, (b) m-Ir/NCNT, (c) l-Ir/NCNT, and (d) Ir (111) surfaces.

uninvolved ($Li^+ + e^-$) pairs because if the reaction step does not include the ($Li^+ + e^-$) pair, the Gibbs free energy cannot be controlled by the applied potential. Among the four independent reaction steps (ΔG_4, ΔG_5, ΔG_{11}, and ΔG_{13}), ΔG_5 was the only step lacking the ($Li^+ + e^-$) pair. The energy differences were negative (−0.498 eV for m-Ir and −0.085 eV for l-Ir) or positive but of small magnitude (0.094 eV for s-Ir and 0.379 eV for Ir (111)) and could be readily overcome at room temperature. We found that both the binding of ($Li^+ + e^-$) (ΔG_4) and the conversion from $LiCO_2^*$ to $Li_2C_2O_4^*$ (ΔG_{11}) were potential limiting steps; therefore, stronger Li* and $Li_2C_2O_4^*$ binding and weaker $LiCO_2^*$ binding (Fig. S10†) would be required to increase the catalytic activity. However, there is usually a binding energy scaling relation between adsorbates sharing the same elements, and it might be difficult to control the binding energy independently.[75,76] Therefore, identifying materials capable of strongly binding ($Li^+ + e^-$) would be an easy way of exploring the periodic table, and the relationship between the Li* binding energy and the catalytic activity of the CRR can be determined.

Similarly, we analyzed the CER mechanism, which was almost identical to the CRR mechanism, except for the opposite sign of the Gibbs free energy. We flipped the signs of all the Gibbs free energy diagrams in Table S2† because we had to consider the reverse reaction (or charging, CER). Nevertheless, the most feasible reaction pathway was identical to that of the CER. Among the four reaction steps ($-\Delta G_4$, $-\Delta G_5$, $-\Delta G_{11}$, and $-\Delta G_{13}$), we considered only three steps ($-\Delta G_4$, $-\Delta G_{11}$, and $-\Delta G_{13}$) to calculate the discharging potential. Unlike in the case of the CRR, we found that there were large energy differences in the initial step of evolution from $2(Li_2CO_3)^* + C^*$ ($-\Delta G_{13}$), specifically, 3.400 eV for s-Ir, 4.014 eV for m-Ir, 6.173 eV for l-Ir, and 6.469 eV for Ir (111). The red discharging plot in Fig. 6 shows an abrupt energy drop in the final step, which involves the generation of a stable discharge product ($Li_2CO_3^*$). This stable and strong binding energy of Li_2CO_3 inhibits the chemical reaction and increases the overpotential. As shown in Fig. 6c and d, Li_2CO_3 preferentially binds to the surface in parallel, increasing the binding area and stability. In contrast, the smaller-sized Ir catalysts loaded on the NCNTs lacked sufficient space to bind properly, which led to a weak binding energy (Fig. S10†). Although the IrO_x/Ir SAC can be strongly bound to Li(s), it provides limited reaction sites to weaken Li_2CO_3 binding due to atomic minimization of the Ir catalysts. Based on the experimental and calculation results, we explored all possible intermediates and pathways to compare the Li–CO_2 performance of the Ir/NCNT systems containing Ir particles of different sizes. We found that the strong binding of ($Li^+ + e^-$) and weak binding of $Li_2CO_3^*$ could be crucial for ensuring excellent catalytic performance of the CRR and CER in Li–CO_2 cells. From these studies, we concluded that the IrO_x/Ir SAC (1.53 V) had the highest (or smallest) potential gap activity, followed by the m- (4.01 V) and l-Ir NPs (6.17 V).

Conclusions

In this study, we introduced an effective strategy to facilitate the Li–CO_2 cell reaction by atomically minimizing IrO_x/Ir bi-phase catalysts uniformly dispersed on NCNT electrodes. We successfully downsized the observable mean catalyst size from 2.69 to 0.42 nm by adjusting the amount of Ir precursors added. In addition to the improved electronic conductivity of N-doped CNTs, N sites doped into CNTs were confirmed to offer stable binding energies, thereby becoming the preferred nucleation sites for Ir catalysts, facilitating fine nucleation instead of particle growth. IrO_x/Ir SACs denoted as s-Ir/NCNTs exhibited a low-intensity Ir peak in their XRD patterns, indicating that a negligible amount of Ir was formed. IrO_x/Ir SACs also exhibited a high IrO_x fraction owing to the presence of dangling

bonds on the Ir surface with a low coordination number, thereby improving the surface catalytic activities. The electrochemical performance of Li–CO_2 cells employing s-Ir/NCNT catalysts was superior to those employing larger sizes and higher loadings of Ir catalysts (m-Ir/NCNTs and l-Ir/NCNTs) as well as pristine NCNTs. The s-Ir/NCNTs exhibited the lowest overpotential of 1.07 V after 30 cycles and stably maintained the low overpotential value even until the 120th cycle, compared to the other samples, which exhibited high overpotentials in a range of 1.5–2 V. We also observed reduced charge transfer resistance at the electrochemical interface as the Ir particle size decreased to a single-atom unit. The reversible formation and decomposition of discharge products were confirmed by *in situ* DEMS characterization of the cells, and s-Ir/NCNTs achieved a higher rate of CO_2 evolution as a result of the reversible decomposition of Li_2CO_3 products. To prove the reaction mechanism and exceptional Li–CO_2 performance of IrO_x/Ir SAC loaded NCNTs, possible intermediates and reaction pathways were investigated by theoretical calculations. We found that the strong binding of $(Li^+ + e^-)$ and weak binding of $Li_2CO_3^*$ could be crucial for maximizing the activity of the catalyst for the reversible Li–CO_2 reaction, and that s-Ir/NCNTs, containing atomic-scale catalysts, can satisfy this requirement and exhibit the lowest overpotential value based on calculations.

Conflicts of interest

There are no conflicts to declare.

Acknowledgements

This work was supported by a National Research Foundation of Korea (NRF) grant funded by the Korean government (MSIT) (No. 2019R1C1C1007886, 2022M3J1A1085410, and 2018R1A5A1025224).

References

1 S. Choi, J. H. Drese and C. W. Jones, *ChemSusChem*, 2009, **2**, 796–854.
2 N. MacDowell, N. Florin, A. Buchard, J. Hallett, A. Galindo, G. Jackson, C. S. Adjiman, C. K. Williams, N. Shah and P. Fennell, *Energy Environ. Sci.*, 2010, **3**, 1645–1669.
3 C. J. Nielsen, H. Herrmann and C. Weller, *Chem. Soc. Rev.*, 2012, **41**, 6684–6704.
4 H. Yamada, *Polym. J.*, 2021, **53**, 93–102.
5 Y. Kim, S. Park, S.-J. Shin, W. Choi, B. K. Min, H. Kim, W. Kim and Y. J. Hwang, *Energy Environ. Sci.*, 2020, **13**, 4301–4311.
6 S. Nitopi, E. Bertheussen, S. B. Scott, X. Liu, A. K. Engstfeld, S. Horch, B. Seger, I. E. Stephens, K. Chan and C. Hahn, *Chem. Rev.*, 2019, **119**, 7610–7672.
7 J. Albo, M. Alvarez-Guerra, P. Castaño and A. Irabien, *Green Chem.*, 2015, **17**, 2304–2324.
8 J. Wu, Y. Huang, W. Ye and Y. Li, *Adv. Sci.*, 2017, **4**, 1700194.
9 D. Sun, X. Xu, Y. Qin, S. P. Jiang and Z. Shao, *ChemSusChem*, 2020, **13**, 39–58.
10 J.-H. Kang, J. Lee, J.-W. Jung, J. Park, T. Jang, H.-S. Kim, J.-S. Nam, H. Lim, K. R. Yoon and W.-H. Ryu, *ACS Nano*, 2020, **14**, 14549–14578.
11 J.-Y. Lee, H.-S. Kim, J.-S. Lee, C.-J. Park and W.-H. Ryu, *ACS Sustainable Chem. Eng.*, 2019, **7**, 16151–16159.
12 H.-S. Kim, J.-Y. Lee, J.-K. Yoo and W.-H. Ryu, *ACS Mater. Lett.*, 2021, **3**, 815–825.
13 Y. Qiao, J. Yi, S. Wu, Y. Liu, S. Yang, P. He and H. Zhou, *Joule*, 2017, **1**, 359–370.
14 B. Liu, Y. Sun, L. Liu, J. Chen, B. Yang, S. Xu and X. Yan, *Energy Environ. Sci.*, 2019, **12**, 887–922.
15 Z. Xie, X. Zhang, Z. Zhang and Z. Zhou, *Adv. Mater.*, 2017, **29**, 1605891.
16 F. Cai, Z. Hu and S. L. Chou, *Adv. Sustainable Syst.*, 2018, **2**, 1800060.
17 H. S. Kim, B. Kim, H. Park, J. Kim and W. H. Ryu, *Adv. Energy Mater.*, 2022, 2103527.
18 S. Ma, Y. Wu, J. Wang, Y. Zhang, Y. Zhang, X. Yan, Y. Wei, P. Liu, J. Wang and K. Jiang, *Nano Lett.*, 2015, **15**, 8084–8090.
19 Y. S. Jeong, J.-B. Park, H.-G. Jung, J. Kim, X. Luo, J. Lu, L. Curtiss, K. Amine, Y.-K. Sun and B. Scrosati, *Nano Lett.*, 2015, **15**, 4261–4268.
20 Y. Hou, J. Wang, J. Liu, C. Hou, Z. Xiu, Y. Fan, L. Zhao, Y. Zhai, H. Li and J. Zeng, *Adv. Energy Mater.*, 2019, **9**, 1901751.
21 Z. Zhang, X. G. Wang, X. Zhang, Z. Xie, Y. N. Chen, L. Ma, Z. Peng and Z. Zhou, *Adv. Sci.*, 2018, **5**, 1700567.
22 X. Zhang, C. Wang, H. Li, X.-G. Wang, Y.-N. Chen, Z. Xie and Z. Zhou, *J. Mater. Chem. A*, 2018, **6**, 2792–2796.
23 Z. Zhang, Z. Zhang, P. Liu, Y. Xie, K. Cao and Z. Zhou, *J. Mater. Chem. A*, 2018, **6**, 3218–3223.
24 S. Li, Y. Liu, J. Zhou, S. Hong, Y. Dong, J. Wang, X. Gao, P. Qi, Y. Han and B. Wang, *Energy Environ. Sci.*, 2019, **12**, 1046–1054.
25 H. Wang, K. Xie, Y. You, Q. Hou, K. Zhang, N. Li, W. Yu, K. P. Loh, C. Shen and B. Wei, *Adv. Energy Mater.*, 2019, **9**, 1901806.
26 J.-S. Lee, H.-S. Kim and W.-H. Ryu, *Appl. Surf. Sci.*, 2019, **466**, 562–567.
27 J.-S. Lee, C. Lee, J.-Y. Lee, J. Ryu and W.-H. Ryu, *ACS Catal.*, 2018, **8**, 7213–7221.
28 W.-H. Ryu, F. S. Gittleson, J. M. Thomsen, J. Li, M. J. Schwab, G. W. Brudvig and A. D. Taylor, *Nat. Commun.*, 2016, **7**, 1–10.
29 K. R. Yoon, D. S. Kim, W. H. Ryu, S. H. Song, D. Y. Youn, J. W. Jung, S. Jeon, Y. J. Park and I. D. Kim, *ChemSusChem*, 2016, **9**, 2080–2088.
30 F. S. Gittleson, W.-H. Ryu, M. Schwab, X. Tong and A. D. Taylor, *Chem. Commun.*, 2016, **52**, 6605–6608.
31 J. Li, A. Dai, K. Amine and J. Lu, *Small*, 2021, **17**, 2007760.
32 L. Zhang, Y. Ren, W. Liu, A. Wang and T. Zhang, *Nat. Sci. Rev.*, 2018, **5**, 653–672.
33 A. Wang, J. Li and T. Zhang, *Nat. Rev. Chem.*, 2018, **2**, 65–81.
34 C. X. Zhao, B. Q. Li, J. N. Liu and Q. Zhang, *Angew. Chem., Int. Ed.*, 2021, **60**, 4448–4463.
35 N. Cheng, L. Zhang, K. Doyle-Davis and X. Sun, *Electrochem. Energy Rev.*, 2019, **2**, 539–573.
36 Q. Zhang and J. Guan, *Adv. Funct. Mater.*, 2020, **30**, 2000768.

37 Y. Zhang, X. Li, M. Zhang, S. Liao, P. Dong, J. Xiao, Y. Zhang and X. Zeng, *Ceram. Int.*, 2017, **43**, 14082–14089.
38 G. Wu, X. Li, Z. Zhang, P. Dong, M. Xu, H. Peng, X. Zeng, Y. Zhang and S. Liao, *J. Mater. Chem. A*, 2020, **8**, 3763–3770.
39 Y. Liu, S. Zhao, D. Wang, B. Chen, Z. Zhang, J. Sheng, X. Zhong, X. Zou, S. P. Jiang and G. Zhou, *ACS Nano*, 2021, **16**, 1523–1532.
40 S. S. A. Shah, T. Najam, M. S. Bashir, L. Peng, M. A. Nazir and M. S. Javed, *Energy Storage Mater.*, 2022, **45**, 301–322.
41 Y. Zhang and W. Yang, *Phys. Rev. Lett.*, 1998, **80**, 890.
42 J. P. Perdew, K. Burke and M. Ernzerhof, *Phys. Rev. Lett.*, 1996, **77**, 3865.
43 B. Hammer, L. B. Hansen and J. K. Nørskov, *Phys. Rev. B*, 1999, **59**, 7413.
44 S. Grimme, J. Antony, S. Ehrlich and H. Krieg, *J. Chem. Phys.*, 2010, **132**, 154104.
45 S. Grimme, S. Ehrlich and L. Goerigk, *J. Comput. Chem.*, 2011, **32**, 1456–1465.
46 C. Yang, K. Guo, D. Yuan, J. Cheng and B. Wang, *J. Am. Chem. Soc.*, 2020, **142**, 6983–6990.
47 Y. Zhai, H. Tong, J. Deng, G. Li, Y. Hou, R. Zhang, J. Wang, Y. Lu, K. Liang and P. Chen, *Energy Storage Mater.*, 2021, **43**, 391–401.
48 A. Ahmadiparidari, R. E. Warburton, L. Majidi, M. Asadi, A. Chamaani, J. R. Jokisaari, S. Rastegar, Z. Hemmat, B. Sayahpour and R. S. Assary, *Adv. Mater.*, 2019, **31**, 1902518.
49 B. Chen, D. Wang, J. Tan, Y. Liu, M. Jiao, B. Liu, N. Zhao, X. Zou, G. Zhou and H.-M. Cheng, *J. Am. Chem. Soc.*, 2022, **144**, 3106–3116.
50 J. K. Nørskov, J. Rossmeisl, A. Logadottir, L. Lindqvist, J. R. Kitchin, T. Bligaard and H. Jonsson, *J. Phys. Chem. B*, 2004, **108**, 17886–17892.
51 I. C. Man, H. Y. Su, F. Calle-Vallejo, H. A. Hansen, J. I. Martínez, N. G. Inoglu, J. Kitchin, T. F. Jaramillo, J. K. Nørskov and J. Rossmeisl, *ChemCatChem*, 2011, **3**, 1159–1165.
52 X. Yu and P. G. Pickup, *J. Power Sources*, 2008, **182**, 124–132.
53 J. Kang, J.-S. Yu and B. Han, *J. Phys. Chem. Lett.*, 2016, **7**, 2803–2808.
54 J. Hummelshøj, J. Blomqvist, S. Datta, T. Vegge, J. Rossmeisl, K. S. Thygesen, A. Luntz, K. W. Jacobsen and J. K. Nørskov, *J. Chem. Phys.*, 2010, **132**, 071101.
55 L. Schick, R. Sanchis, V. González-Alfaro, S. Agouram, J. M. López, L. Torrente-Murciano, T. García and B. Solsona, *Chem. Eng. J.*, 2019, **366**, 100–111.
56 M. Bou, J. Martin, T. Le Mogne and L. Vovelle, *Appl. Surf. Sci.*, 1991, **47**, 149–161.
57 S. Delpeux, F. Beguin, R. Benoit, R. Erre, N. Manolova and I. Rashkov, *Eur. Polym. J.*, 1998, **34**, 905–915.
58 N. Ghali, C. Vivien, B. Mutel and A. Rives, *Surf. Coat. Technol.*, 2014, **259**, 504–516.
59 D. Rats, L. Vandenbulcke, R. Herbin, R. Benoit, R. Erre, V. Serin and J. Sevely, *Thin Solid Films*, 1995, **270**, 177–183.
60 Y. Xu, Y. Mo, J. Tian, P. Wang, H. Yu and J. Yu, *Appl. Catal., B*, 2016, **181**, 810–817.
61 R. Czerw, M. Terrones, J.-C. Charlier, X. Blase, B. Foley, R. Kamalakaran, N. Grobert, H. Terrones, D. Tekleab and P. Ajayan, *Nano Lett.*, 2001, **1**, 457–460.
62 K. Gong, F. Du, Z. Xia, M. Durstock and L. Dai, *science*, 2009, **323**, 760–764.
63 X. Li, J. Zhou, J. Zhang, M. Li, X. Bi, T. Liu, T. He, J. Cheng, F. Zhang and Y. Li, *Adv. Mater.*, 2019, **31**, 1903852.
64 H.-D. Lim, Y. S. Yun, S. Y. Cho, K.-Y. Park, M. Y. Song, H.-J. Jin and K. Kang, *Carbon*, 2017, **114**, 311–316.
65 T. S. Marinova and K. Kostov, *Surf. Sci.*, 1987, **181**, 573–585.
66 M. Rubel, R. Haasch, P. Mrozek, A. Wieckowski, C. De Pauli and S. Trasatti, *Vacuum*, 1994, **45**, 423–427.
67 M. Wittmer, P. Oelhafen and K.-N. Tu, *Phys. Rev. B*, 1986, **33**, 5391.
68 J. Zhu and S. Mu, *Chem. Commun.*, 2021, **57**, 7869–7881.
69 Y. Wang, X. Cui, L. Peng, L. Li, J. Qiao, H. Huang and J. Shi, *Adv. Mater.*, 2021, **33**, 2100997.
70 X. Luo, M. Yang, W. Song, Q. Fang, X. Wei, L. Jiao, W. Xu, Y. Kang, H. Wang and N. Wu, *Adv. Funct. Mater.*, 2021, **31**, 2101193.
71 N. Sun, H. Liu, Z. Yu, Z. Zheng and C. Shao, *Ionics*, 2016, **22**, 869–876.
72 W.-H. Ryu, F. S. Gittleson, J. Li, X. Tong and A. D. Taylor, *Nano Lett.*, 2016, **16**, 4799–4806.
73 Y. I. Choi, H. Park, G.-P. Kim, D. Lim, J. Jang, S. E. Shim, S. H. Park and S.-H. Baeck, *J. Nanosci. Nanotechnol.*, 2016, **16**, 10459–10464.
74 W. M. Irvine, in *Encyclopedia of Astrobiology*, ed. M. Gargaud, R. Amils, J. C. Quintanilla, H. J. Cleaves, W. M. Irvine, D. L. Pinti and M. Viso, Springer Berlin Heidelberg, Berlin, Heidelberg, 2011, pp. 905–905, DOI: **10.1007/978-3-642-11274-4_863**.
75 Y. Li and Q. Sun, *Adv. Energy Mater.*, 2016, **6**, 1600463.
76 J. K. Nørskov, F. Abild-Pedersen, F. Studt and T. Bligaard, *Proc. Natl. Acad. Sci.*, 2011, **108**, 937–943.